APPLIED RESEARCH

WILEY

Effects of tumour heterogeneous properties on modelling the transport of radiative particles

Victor Ogesa Juma[1] | Diego Sainz-DeMena[1] | María Teresa Sánchez[2,3] | José Manuel García-Aznar[1]

[1]Mechanical Engineering Department, Multiscale in Mechanical and Biological Engineering, Aragon Institute of Engineering Research (I3A), University of Zaragoza, Zaragoza, Spain

[2]Centro Universitario de la Defensa de Zaragoza, Zaragoza, Spain

[3]Instituto Universitario de Investigación en Matemáticas y Aplicaciones (IUMA), Universidad de Zaragoza, Zaragoza, Spain

Correspondence
José Manuel García-Aznar, Multiscale in Mechanical and Biological Engineering, Aragon Institute of Engineering Research (I3A), University of Zaragoza, 50018 Zaragoza, Spain.
Email: jmgaraz@unizar.es

Abstract

Dose calculation plays a critical role in radiotherapy (RT) treatment planning, and there is a growing need to develop accurate dose deposition models that incorporate heterogeneous tumour properties. Deterministic models have demonstrated their capability in this regard, making them the focus of recent treatment planning studies as they serve as a basis for simplified models in RT treatment planning. In this study, we present a simplified deterministic model for photon transport based on the Boltzmann transport equation (BTE) as a proof-of-concept to illustrate the impact of heterogeneous tumour properties on RT treatment planning. We employ the finite element method (FEM) to simulate the photon flux and dose deposition in real cases of diffuse intrinsic pontine glioma (DIPG) and neuroblastoma (NB) tumours. Importantly, in light of the availability of pipelines capable of extracting tumour properties from magnetic resonance imaging (MRI) data, we highlight the significance of such data. Specifically, we utilise cellularity data extracted from DIPG and NB MRI images to demonstrate the importance of heterogeneity in dose calculation. Our model simplifies the process of simulating a RT treatment system and can serve as a useful starting point for further research. To simulate a full RT treatment system, one would need a comprehensive model that couples the transport of electrons and photons.

KEYWORDS

Boltzmann transport equation, DIPG, finite element method, mathematical modelling, neuroblastoma, numerical methods, photon transport, radiative particle transport

1 | INTRODUCTION

The most common methods in cancer therapy are surgery, chemotherapy and radiotherapy (RT).[1] RT uses high doses of radiation to kill cancer cells and shrink tumours by exposing them to high-energy rays.[2] The radiation kills cancer cells or damages their DNA, hence slowing down their growth. Cancer cells whose DNA is damaged beyond repair stop dividing or die. When the damaged cells die, they are broken down and removed by the body.[3]

During RT treatment, the source of radiation may be outside the body (external RT or teletherapy) or inside the body and very close to the tumour (internal RT or brachytherapy). External RT uses high-energy (ionising) radiations to damage and destroy cancer cells and tumours. The high energy absorbed in the body is measured in doses (Gy), hence the need for dose calculation models. The first and widely used models for clinical dose calculation were the semi-empirical methods, pencil-beam, convolution superposition and the statistical model based on the Monte Carlo method.[4,5] The use of deterministic methods based on modelling particle transport within a medium were not widely used at first but they have gained attention during the last decades in RT treatment planning.[6,7] These methods form the basis upon which simplified models for RT treatment planning can be developed, guaranteeing a fast and accurate planning system.[4,6,7] Börgers[8] showed that numerical methods for linear BTE with high degree of accuracy are competitive to Monte Carlo dose calculation model. To achieve a desirable accuracy of the delivered dose to the tissue, it is recommended that the dose distribution uncertainty should not exceed 2%.[9,10] Although the dose distributions arising from the solution of BTE are accurate and comparable to those obtained from Monte Carlo simulations, initially there was less use of BTE in the RT treatment planning due to their high dimensional nature (the steady state BTE is six dimensional; three for spatial, two for angular and one for energy variables, respectively); however, due to the increase in computational power and capacity, there has been an increasing use of these methods. In particular, Acuros was the first algorithm of this type to be implemented in a commercial treatment planning system.[7,11] More recently, St. Aubin et al[12] developed a new algorithm for solving the Boltzmann equation applicable to dose calculations for MRI-guided RT systems.

The problem of dose calculation is divided into two parts: the forward and the inverse problems. The forward problem focuses on calculating the photon flux within the body, which enables computing the absorbed dose into the body, and hence tumour response to radiations given fixed parameter values and machine set up. The inverse problem, which is an optimization problem, requires first to correctly define the forward problem. Therefore, this work is focused on the numerical simulation of this forward problem, where the absorbed dose within the body can then be calculated from the fluxes of low energy particle (photon), as a representative of a brachytherapy treatment planning. In this study, the focus is on modelling the dose distribution in brachytherapy treatment using low-energy photon fluxes. To simplify the problem, we make certain assumptions. First, we assume that photons scatter isotropically, meaning they scatter in all directions equally. Additionally, we assume that the photons experience only a few scattering and collision events as they travel through the medium. These assumptions are valid for low-energy photon transport.[13] By adopting these simplifications, we aim to streamline the modelling process and obtain insights into the dose distribution during brachytherapy treatment. Furthermore, this approach can be extended to model a comprehensive transport system that encompasses the transport of high-energy electron, photon and positron particles; however, a comprehensive treatment system is beyond the scope of this study.

Since many years ago, linear Boltzmann transport equations (LBTE) have been used in the study of particle transport.[14,15] In the last two decades, the interest in the application of BTE as a dose calculation model in RT has increased.[4,16,17] Several studies have not only focused on the simplification of BTE for dose calculation, but also methods of approximating the solution of BTE. Such methods which have been used in literature to approximate the solutions of BTE include: finite element method (FEM) for spatial variable, multi-group methods for energy and discrete-ordinate method, spherical harmonics, moment methods and expansion in orders of scattering for angular domain.[6,7,16–20] Vassilev et al[7] presented the use of deterministic solver Acuros for coupled photon-electron linear BTE equation and compared this to Monte Carlo methods for homogeneous and heterogeneous domains. In this work, discontinuous FEM was used to discretise spatial variable, multi-group method for energy and discrete-ordinate method for angle. Boman et al[16,17] solved numerically the linear steady-state BTE by applying FEM to all the state variables, and illustrated this using simplified geometries. Their solutions found reasonable agreement with Monte Carlo simulations. Moreover, Hensel et al[20] compared their calculation on simple geometries with tabulated Cobalt-60 depth dose curves and found a good comparison to Monte Carlo method. Additionally, Das and Pouso[13] applied the method based on the expansion in orders of scattering to approximate the solution of the steady-state linear BTE for photons and illustrated the solution on a regular rectangular-shaped geometry. To add on, there are other techniques which combine FEM together with discrete ordinate method for other variables. Gifford et al[6] presented the numerical solution of BTE by discretizing the spatial and angular domains using FEM while applying discrete-ordinate method to the energy domain. Tervo et al[15] presented the solution of continuous slowing down approximation (CSD) of BTE by applying finite element (FE) discretization on all the six variables by considering separable shape functions and implemented this on an ideal two-dimensional (2D) geometry.

An important aspect in dose calculation is the integration of tissue and tumour heterogeneous characteristics in the dose calculation models. Cancerous tumours have shown to be very complex and heterogeneous in nature, with their heterogeneity stemming from the growth control parameters, metastasis and cell characteristics. Among the contributors to tumour heterogeneity is the cellularity and vascularization. Mathematical models of dose calculation involving heterogeneous properties are believed to increase accuracy in RT treatment planning. Different research studies in this area focus on different heterogeneous properties.[21–24] Poon et al[23] accounted for shielding heterogeneity and patient boundaries through the Monte Carlo simulations for high-dose-rate endorectal brachytherapy (HDREBT), while Richardson et al[24] studied the impact of air gaps around vaginal cylinders as a source of heterogeneity in patients. Celora et al[21] showed that RT poor treatment outcomes was as a result of tumour heterogeneity. Mikell et al[22] studied the differences in the doses calculated based on commercial grid-based Boltzmann equations solver, Acuros, which includes tissue heterogeneity in the algorithm and compared this to the standard dose estimates for cervical cancer patients, with the differences in results accounting for heterogeneous properties. Therefore, there is need to better understand how the dose distribution is affected by heterogeneous properties of tumour and the surrounding tissue. In this work, we aim to highlight the impact of heterogeneous properties on the solution of a simplified case of the LBTE for low energy photon transport with assumed isotropic scattering. Specifically, we investigate the influence of cellularity data as a source of heterogeneity, where we use a mathematical model for photon transport with limited scattering events. For a full treatment system, a compressive model incorporating transport of photons, electrons and positrons should be used. Figure 1 shows the heterogeneous cellularity distribution in clinical cases of neuroblastoma (NB; top panel) and diffuse intrinsic pontine glioma (DIPG; bottom panel) tumours. As shown from the figure, NB tumour is
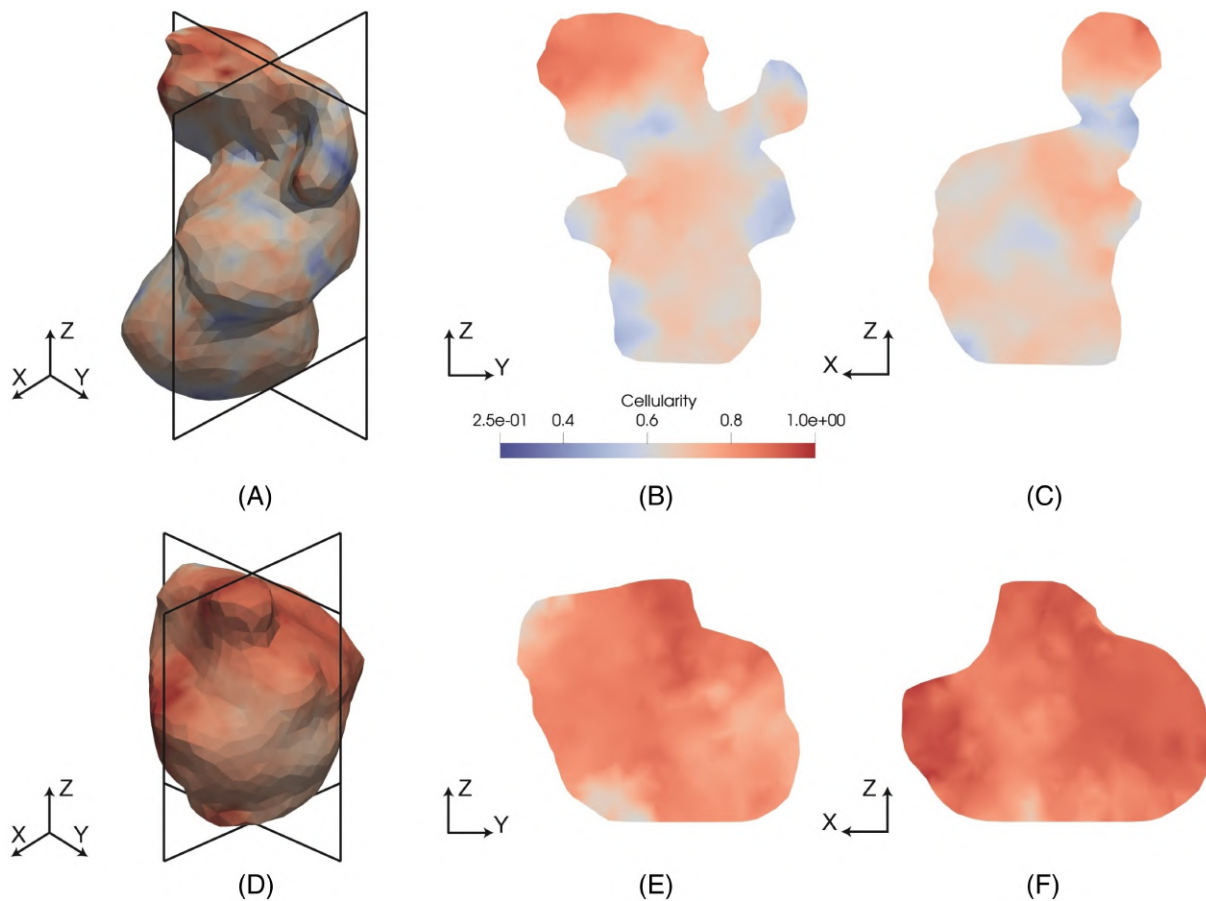

FIGURE 1 Heterogeneous distribution of cellularity in FE meshes generated from clinical images of DIPG and NB tumours, viewed through different planes. figures (b) and (c), respectively (e) and (f) are cut views of the tumours, with the planes used for these cuts shown in figures (a) and (d), respectively. *Top panel*: Cellularity distribution in a NB tumour (a) whole three-dimension (3D) tumour (b) viewed through the *y-z* plane; (c) viewed from the *x-z* plane. *Bottom panel*: Cellularity distribution in a DIPG tumour (c) whole DIPG tumour; (d) viewed through the *y-z* plane; (e) viewed from the *x-z* plane. DIPG, diffuse intrinsic pontine glioma; FE, finite element; NB, neuroblastoma.

more heterogeneous than DIPG, and we shall see later how these differences account for the differences in dose distributions in the two types of tumours.

In this work, we therefore, formulate the forward problem of radiative particle flux of photons using BTE and then use continuous FEM to approximate the photon flux within a medium for the case of brachytherapy, where for simplicity, we assume that the scattering is isotropic and only low energy levels are used. In addition, the solution is approximated using the FEM to all the variables and illustrated on an irregular geometry of a real clinical case of a specific patient with a tumour that requires RT as the only possible treatment, as it is the DIPG cases, obtained within the context of PRIMAGE project.[25] Additionally, we also apply this to a real clinical case of a patient with NB tumour, which sometimes also requires RT as a means of management and treatment. Furthermore, we introduce tumour heterogeneity into the dose calculation models, hence highlighting the importance of incorporating tumour heterogeneous properties into such models. NB tumour is more heterogeneous than DIPG, therefore, we used both real cases of the two types of tumours to comment on the dose distribution differences due to heterogeneous properties. To incorporate heterogeneous properties, we used the available cellularity information data, which we assume is proportional to the cell density of the tumour. There are more tissue properties that affect dose distribution in addition to cellularity, such as extracellular matrix (ECM) density or interstitial fluid pressure. However, due to the limited availability of data in clinical practice, in this work we have focused on cellularity. Thus, we consider this variable as representative of tissue heterogeneity. While it may not be directly correlated with the other variables we have named, given the limitations explained and the relation between cellularity and tissue density, we consider cellularity as the main source of tissue heterogeneity. The data was extracted using the workflow developed by members from our research group,[26] that analyses clinical images and generates a three-dimensional (3D) FE mesh together with the interpolated data. Specifically, the available data included a T2-weighted magnetic resonance imaging (MRI) series where the tumour was manually segmented by experienced radiologists, as well as a diffusion weighted (DW) MRI sequence. Using the segmentations as a starting point, we reconstructed the 3D geometry of the tumour. To accomplish this, we extracted the contours of each segmented image and applied interpolation techniques to generate a point cloud that represents the surface shape in 3D. Using this cloud, we proceeded to construct the surface and volumetric FE mesh of the tumour, which will be utilised for simulations. This task was performed with the assistance of the im2mesh Python library.[26] Once the geometries were generated, DW-MRI sequences were analysed to evaluate the cellularity levels of the tumours. Apparent diffusion coefficient (ADC) maps are obtained from this type of MRI sequences. This variable measures the Brownian motion of water molecules in the tissue. Depending on the cellularity level of this tissue, the ADC will change. To get an estimate of the cellularity volume fraction, we employ the equation proposed by Atuegwu et al[27]:

$$\text{Cellularity} = \left(\frac{\text{ADC}_\text{w} - \text{ADC}}{\text{ADC}_\text{w} - \text{ADC}_\text{min}} \right). \tag{1}$$

Figure 1 illustrates extrapolated heterogeneous distribution of the cellularity of real clinical cases of DIPG and NB tumours used in this work. This study, though applied to a simplified case of low energy photons which are assumed to scatter isotropically for brachytherapy, forms our building block on integrating the BTE to the model of tumour growth (see Reference 28 for some studies involving tumour growth model applied to NB), to simulate tumour dynamics following the RT treatment.

Hence, the rest of this article is organised as follows. In Section 2, we present a deterministic model for dose calculation, described by the BTE, after which we describe the FE discretization and the concept of separable shape functions which is used in this article. In Section 3, we discuss the examples of application of BTE in ideal cases in 2D and 3D and two examples of real tumours (DIPG and NB). Section 4 focuses on the results of BTE in the examples of applications and real tumours, where we assumed a single radiation source placed close to the tumour, or a double source of radiation to the tumour; in this section, we also incorporate heterogeneous properties into the dose model and hence highlighting their importance. This article wraps with a discussion and conclusions in Section 5, including also the limitations of this study.

2 | BOLTZMANN TRANSPORT EQUATIONS

In this section, we describe linear BTEs for one particle, applied to RT. In this study, we limit our formulation and hence discussion to the transport of low energy neutral (photon) particles. LBTE is a form of BTE that ignores

particles' interaction with each other, and only assumes that they interact with the matter as they pass through them; we further discuss the discretization by continuous FEM with separable basis functions that we use to fully solve LBTE in all the spatial, angular and energy variables. Continuous FEM can produce instabilities, and therefore, we have used streamline-diffusion approach to stabilise the solution. As an illustration of the separable shape functions, we only present a case of two dimensions. The 3D description and equations can be presented analogously. Furthermore, we describe a model for dose deposition based on the total energy released per unit mass at the point of photon interaction. This approximation is in line with our assumption of low energy photon transport with isotropic scattering. For full description of external RT, where the scattering is non-isotropic, this assumption might not be not valid.

2.1 | Transport equations

The BTE is a seven-dimensional integro-partial differential equation that describes the transport of charged particles whose flux is denoted by ψ and defined at the spatial position $\mathbf{x}$, travelling with velocity Ω and with energy E.[29,30] The equation is based on the particle conservation within a medium.[31] In RT treatment, linear steady state BTE is used since the speed of radiative particles is much faster, hence the steady state is achieved much faster.[16] This assumption eliminates the time variable, hence reducing the number of dimensions of BTE to 6. In order to simplify the mathematical analysis and increase computational efficiency, several approximate models derived from BTE were proposed. These include Fokker–Planck and CSD approximations.[9,15,32,33] This study focuses only on the low energy photon transport in a medium, which we assume they deposit the energy locally at the point of interaction.[7,34]

To describe the BTE model, we assume a spatial domain V as shown in Figure 2. The boundary of the domain, denoted ∂V, is decomposed to distinguish front and rear boundaries such that $\partial V = \partial V_1 \cup \partial V_2$, where ∂V_1 and ∂V_2 are the respective front and rear boundaries of the spatial domain. We define a patch Γ on ∂V_1, where there is influx of particles into domain (point where the source of radiation to the tumour is placed), hence, on Γ we set $\psi = \psi_0$, which represents the particles flux per unit area incident on Γ. This flux travels with angular velocity Ω. On ∂V_1, the requirement that $\mathbf{n}(\mathbf{x}) \cdot \Omega < 0$ must be satisfied, being $\mathbf{n}(\mathbf{x})$ the unit outward normal vector to the surface ∂V at the point $\mathbf{x}$. The condition $\mathbf{n}(\mathbf{x}) \cdot \Omega < 0$ helps distinguish front boundary from the rear. A point $\mathbf{x}$ lies on the rear boundary if the condition $\mathbf{n}(\mathbf{x}) \cdot \Omega > 0$ is satisfied. In formulating BTE for dose calculation, we also assume that the domain is convex, which means that a particle can only enter the domain once. Although some particles may re-enter the domain due to scattering and collision effects, this contribution is negligible and hence ignored in this study.
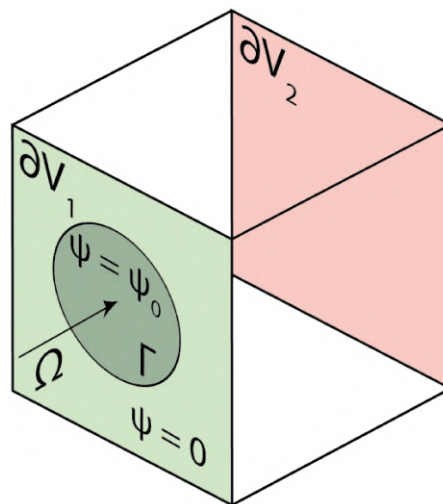

FIGURE 2 A schematic representation of the spatial domain illustrating the front (∂V_1) and rear (∂V_2) boundaries. The incoming radiation source with surface incident flux ψ_0, travelling with velocity Ω are placed close to the circular patch (Γ), while in the remaining section of ∂V_1, there is no radiation source $\psi_0 = 0$.

The BTE of photon together with the boundary conditions are defined by:

$$\Omega \cdot \nabla \psi(\mathbf{x}, E, \Omega) + K\psi(\mathbf{x}, E, \Omega) = Q(\mathbf{x}, E, \Omega), \quad \text{in } V \times I \times S, \tag{2a}$$

$$\psi = \begin{cases} 0 & \text{for}(\mathbf{x}, E, \Omega) \in \partial V \backslash \Gamma \times I \times S: \ \mathbf{n}(\mathbf{x}) \cdot \Omega < 0 \\ \psi_0 & \text{for}(\mathbf{x}, E, \Omega) \in \Gamma \times I \times S: \ \mathbf{n}(\mathbf{x}) \cdot \Omega < 0 \end{cases} \quad \text{on } \partial V_1 \tag{2b}$$

$$K\psi = \sigma_t(x, E, \Omega)\psi(x, E, \Omega) - \int_I \int_S \sigma_s(\mathbf{x}, E', E, \Omega', \Omega)\psi(x, E', \Omega')dE'd\Omega' \tag{2c}$$

where $\mathbf{x} = (x,y,z)$ and ∂V is the spatial boundary, while I and S are the respective energy and angular domains. The term $\Omega \cdot \nabla \psi(\mathbf{x}, E, \Omega)$ represents the particle transport, $K\psi$ defined in Equation (2c) is the interaction term, defined in terms of differential and total cross-sections, denoted respectively by $\sigma_s(\mathbf{x}, E', E, \Omega', \Omega)$ and $\sigma_t(\mathbf{x}, E, \Omega)$. The differential cross-section is defined as the probability per unit path length for a particle about the point $(\mathbf{x}, E, \Omega)$ with an incoming energy E' and incoming velocity Ω' to scatter into an energy dE and velocity (angle) $d\Omega$; while the total cross-section is the integration of differential cross-sections for absorbed and scattered particles over the energy and angle intervals. $Q(\mathbf{x}, E, \Omega)$ represents the source term, which for this case is set to zero, hence the source of particles being the set Cauchy boundary conditions. An alternative formulation could be to let the Cauchy (initial) boundary conditions be absorbed into the source term, however, this is not implemented here. The interaction term, represented as $K\psi$, Equation (2c) can be determined by using existing explicit formulations for the differential cross-section available in the literature, such as those described in References 17,35. Alternatively, one can obtain the differential cross-sectional data for photons from the National Institute of Standard and Technology (NIST) LAB.[36] By selecting the desired material, it is possible to extract various cross-sections of interest.

To provide an illustration, we extracted and visualised different cross-sections and scattering events for photons propagating through a water medium within the energy range of [0.01,100], as depicted in Figure 3. The cross-sectional data presented in this figure, except for the pair production, which occurs at high energy, were employed in our numerical simulations for evaluating photon fluxes and dose deposition.

2.2 | Finite element method

We solve Equation (2) by applying FEM to all the variables: spatial $\mathbf{x}$, angular Ω and energy E. We follow the approach used in References 15,17, which we just present here for completeness.
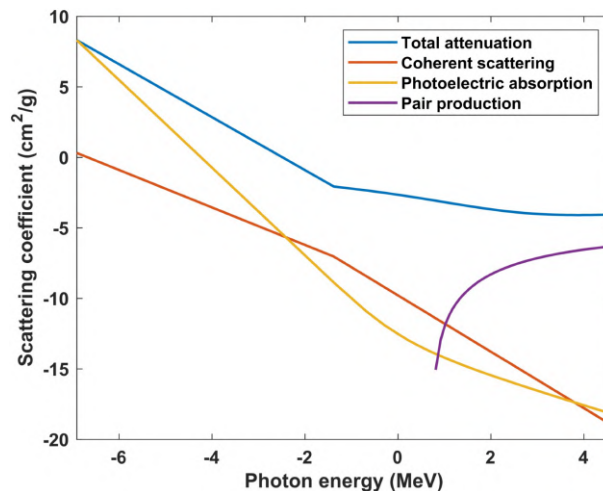

FIGURE 3 Different scattering cross-sections for photon interactions in a water medium at different energies plotted in log scale. The cross-sectional data was obtained from NIST LAB.[36]

Let us first define the integral operator,

$$\langle u,v \rangle = \int_V \int_I \int_S u(\mathbf{x},E,\Omega)v(\mathbf{x},E,\Omega)d\Omega dEdV,$$

therefore, the variational form of Equation (2) is given by;

$$\langle \Omega \cdot \nabla \psi, u \rangle + \langle K\psi, u \rangle = \langle Q,u \rangle, \tag{3}$$

where u is a test function in the domain $V \times I \times S$.

Applying Green's theorem on the first term,

$$\langle \Omega \cdot \nabla \psi, u \rangle = -\langle \psi, \Omega \cdot \nabla u \rangle + \int_{\partial V} \int_I \int_S (\Omega \cdot \mathbf{n})\psi u d\Omega dEd\mathbf{x}_{\partial \mathbf{V}},$$

we can rewrite the variational formulation as

$$-\langle \psi, \Omega \cdot \nabla u \rangle + \int_I \int_S \int_{\partial V} (\Omega \cdot \mathbf{n})\psi u d\Omega dEd\mathbf{x}_{\partial \mathbf{V}} + \langle K\psi, u \rangle = \langle Q,u \rangle. \tag{4}$$

We split the boundary to fully characterise the front and rear boundaries, taking note of the fact that the initial flux ψ_0 is zero everywhere on the front boundary except on the patch Γ, as follows:

$$\int_I \int_S \int_{\partial V} (\Omega \cdot \mathbf{n})\psi u d\Omega dEd\mathbf{x}_{\partial \mathbf{V}} = \int_I \int_S \int_{\partial V} \left[(\Omega \cdot \mathbf{n})_+ - (\Omega \cdot \mathbf{n})_- \right]\psi u d\Omega dEd\mathbf{x}_{\partial \mathbf{V}}, \tag{5a}$$

$$= \int_I \int_S \int_{\partial V_2} (\Omega \cdot \mathbf{n})_+ \psi u d\Omega dEd\mathbf{x}_{\partial \mathbf{V}} - \int_I \int_S \int_\Gamma (\Omega \cdot \mathbf{n})_- \psi_0 u d\Omega dEd\mathbf{x}_{\partial \mathbf{V}}, \tag{5b}$$

where the negative $(-)$ or positive $(+)$ subscripts indicate the sign of $(\Omega \cdot \mathbf{n})$. In this set-up, we define the domain as $D = V \times I \times S$, therefore if $\overline{V}$ is the closure of V, we denote $\overline{D} = \overline{V} \times I \times S$, and define $W \subset \mathcal{C}(D)$ as the space of continuous functions on $\overline{D}$. Therefore, combining Equations (4) and (5), the variational form of Equation (2) together with the boundary conditions takes the form, find $\psi, u \in W$ such that:

$$B(\psi,u) = F(u), \tag{6}$$

where the bilinear form $B(\psi,u)$ is,

$$B(\psi,u) = -\langle \psi, \Omega \cdot \nabla u \rangle + \int_I \int_S \int_{\partial V_2} (\Omega \cdot \mathbf{n})_+ \psi u d\Omega dEd\mathbf{x}_{\partial \mathbf{V}} + \langle K\psi, u \rangle$$

and

$$F(u) = \langle Q,u \rangle + \int_I \int_S \int_\Gamma (\Omega \cdot \mathbf{n})_- \psi_0 u d\Omega dEd\mathbf{x}_{\partial \mathbf{V}}.$$

The convergence and stability of the FEM for the transport model and the existence and stability of the solution of variational form (6) were established in the previous published works[17,37,38] and hence are not covered here. Next, we used FEM to find the weak solution $\psi \in W$ of (2). Let $W_1 \subset W$ be finite dimensional such that $W_1 = [u_1, u_2, \cdots, u_N]$, we consider different basis functions for different subdomains; for spatial domain, we use linear triangular elements for 2D geometry, and linear tetrahedron elements for a 3D geometry; similarly for angular subdomain in 3D, which is the surface of a sphere, we use triangular elements, and in case of the circumference of a circle, the elements are sub-intervals,

similar to the energy domain. The FE approximation of the solution ψ is therefore, a linear combination of the test functions $u_i, i = 1, 2, \cdots, N$ given by:

$$\psi_w(\mathbf{x}, E, \Omega) = \sum_{i=1}^{N} \alpha_i u_i(\mathbf{x}, E, \Omega), \quad \forall u \in W_1,$$

and satisfies

$$B(\psi_w, u) = F(u). \tag{7}$$

Using these basis functions as test functions, variational problem (7) becomes, find α such that

$$A\alpha = b \text{ where } A = A_1 + A_2 + A_3, b = b_1 + b_2, \alpha = (\alpha_1, \alpha_2, \cdots, \alpha_N)^T \text{ and} \tag{8}$$

$$A_1(j, i) = -\langle u_i, \Omega \cdot \nabla u_j \rangle \tag{9a}$$

$$A_2(j, i) = \int_I \int_S \int_{\partial V} (\Omega \cdot \mathbf{n})_+ u_i u_j d\Omega dE d\mathbf{x}_{\partial \mathbf{V}} \tag{9b}$$

$$A_3(j, i) = \langle K u_i, u_j \rangle \tag{9c}$$

$$b_1(j) = \int_I \int_S \int_{\partial V} (\Omega \cdot \mathbf{n})_- \psi_0 u_j d\Omega dE d\mathbf{x}_{\partial \mathbf{V}}, \quad b_2(j) = \langle Q, u_j \rangle \tag{9d}$$

Due to the presence of gradient terms, the linear system (8) may produce instabilities in its solution. Therefore, to stabilise the solutions and speed up the convergence, the proposed algorithm is to use diffusion like smoothing approach as described in References 39–41. In this method, a test function of the form $u + \delta \Omega \cdot \nabla u$ is used, where the constant δ is chosen to depend on spatial discretization.[40] This allows us to derive the modified linear system. Multiplying Equation (2) by the test function $u + \delta \Omega \cdot \nabla u$ and following similar procedure as before, we get the following variational problem;

$$B(\psi, u) = F(u), \tag{10}$$

where the bilinear form $B(\psi, u)$, because of streamline-diffusion method changes to,

$$B(\psi, u) = -\langle \psi, \Omega \cdot \nabla u \rangle + \int_I \int_S \int_{\partial V_2} (\Omega \cdot \mathbf{n})_+ \psi u d\Omega dE d\mathbf{x}_{\partial \mathbf{V}}$$
$$+ \langle K\psi, u \rangle + \langle \Omega \cdot \nabla \psi + K\psi, \delta \Omega \cdot \nabla u \rangle$$

and

$$F(u) = \langle Q, u + \delta \Omega \cdot \nabla u \rangle + \int_I \int_S \int_{\Gamma} (\Omega \cdot \mathbf{n})_- \psi_0 u d\Omega dE d\mathbf{x}_{\partial \mathbf{V}}.$$

Similarly to the previous variational formulation, FEM is used to find the weak solution $\psi \in W$ of (2) with streamline-diffusion method. The FE approximation of the solution ψ is therefore, a linear combination of the test functions $u_i, i = 1, 2, \cdots, N$ given by:

$$\psi_w(\mathbf{x}, E, \Omega) = \sum_{i=1}^{N} \alpha_i u_i(\mathbf{x}, E, \Omega), \quad \forall u \in W_1,$$

and satisfies

$$B(\psi_w, u) = F(u). \tag{11}$$

Using these basis functions as test functions, variational problem (11) can be written as a system of linear equations, find α such that

$$A\alpha = b \text{ where } A = A_1 + A_2 + A_3 + A_4 + A_5, \tag{12a}$$

$$b = b_1 + b_2 + b_3, \tag{12b}$$

$$\alpha = (\alpha_1, \alpha_2, \cdots, \alpha_N)^T, \tag{12c}$$

and

$$A_1(j,i) = -\langle u_i, \Omega \cdot \nabla u_j \rangle \tag{13a}$$

$$A_2(j,i) = \int_I \int_S \int_{\partial V} (\Omega \cdot \mathbf{n})_+ u_i u_j d\Omega dE d\mathbf{x}_{\partial \mathbf{V}}, \quad A_3(j,i) = \langle K u_i, u_j \rangle \tag{13b}$$

$$A_4(j,i) = \langle \Omega \cdot \nabla u_i, \delta \Omega \cdot \nabla u_j \rangle, \quad A_5(j,i) = \langle K u_i, \delta \Omega \cdot \nabla u_j \rangle \tag{13c}$$

$$b_1(j) = \int_I \int_S \int_{\partial V} (\Omega \cdot \mathbf{n})_- \psi_0 u_j d\Omega dE d\mathbf{x}_{\partial \mathbf{V}}, \quad b_2(j) = \langle Q, u_j \rangle, \quad b_3(j) = \langle Q, \delta \Omega \cdot \nabla u_j \rangle \tag{13d}$$

For simplicity, we let $Q = 0$ such that $b_2(j) = 0$ and $b_3(j) = 0$. This ensures that the photons source is from a radiation source placed close to the tumour domain. To solve the system of linear equations (12) with separable basis functions, we define the continuous shape functions as a tensor product of basis functions in spatial, angular and energy domains, respectively. Having previously assumed that we consider transport of low energy photons, with isotropic scattering, here we are justified to use continuous basis function, despite the possible lack of accuracy in a general case. This method allows us to calculate smaller matrices in the respective spatial, angle and energy grids, after which their Kronecker tensor product is obtained for solving the resulting linear system. The method of separable basis functions therefore allows discretization of spatial, angular and energy domains independently.

In order to illustrate how separable shape functions are used, we consider a typical case of 2D spatial geometry, and with the photon flux velocity in the direction of unit vector in polar coordinate system (partitions of the circumference of a circle). This method can analogously be extended to a 3D spatial geometry with photon flux velocity proportional to unit vector in spherical coordinate system (partitions of the surface of a sphere). Figure 4 illustrates the separated grids for a 2D case, with the meshed rectangular spatial domain, angular domain in 1D, $[0, 2\pi]$ subdivided into 25 nodes and the energy interval $[0, 1]$ subdivided into 10 energy levels. This figure shows typical coarse grids in each domain for illustrative purposes. We remark that for realistic RT treatment problem, one needs finer meshes to increase accuracy of the solutions. This however results in an increased storage and simulation time, therefore, there has to be some trade-off between accuracy, efficiency and computational speed.

For a 2D simulation, we take the angular directions as a unit vector $\Omega(\theta) = \cos\theta \widehat{\mathbf{i}} + \sin\theta \widehat{\mathbf{j}}$ and hence the line integral on a circle becomes,

$$\int_S g(\Omega) d\Omega = \int_0^{2\pi} g \circ \Omega(\theta) d\theta.$$

To use separable basis functions, we write

$$u_i(\mathbf{x}, E, \Omega) = u_{i_x}^x(\mathbf{x}) u_{i_e}^E(E) u_{i_a}^\Omega(\Omega), \quad \text{with} \quad i = 1, 2, \cdots, N, \tag{14}$$
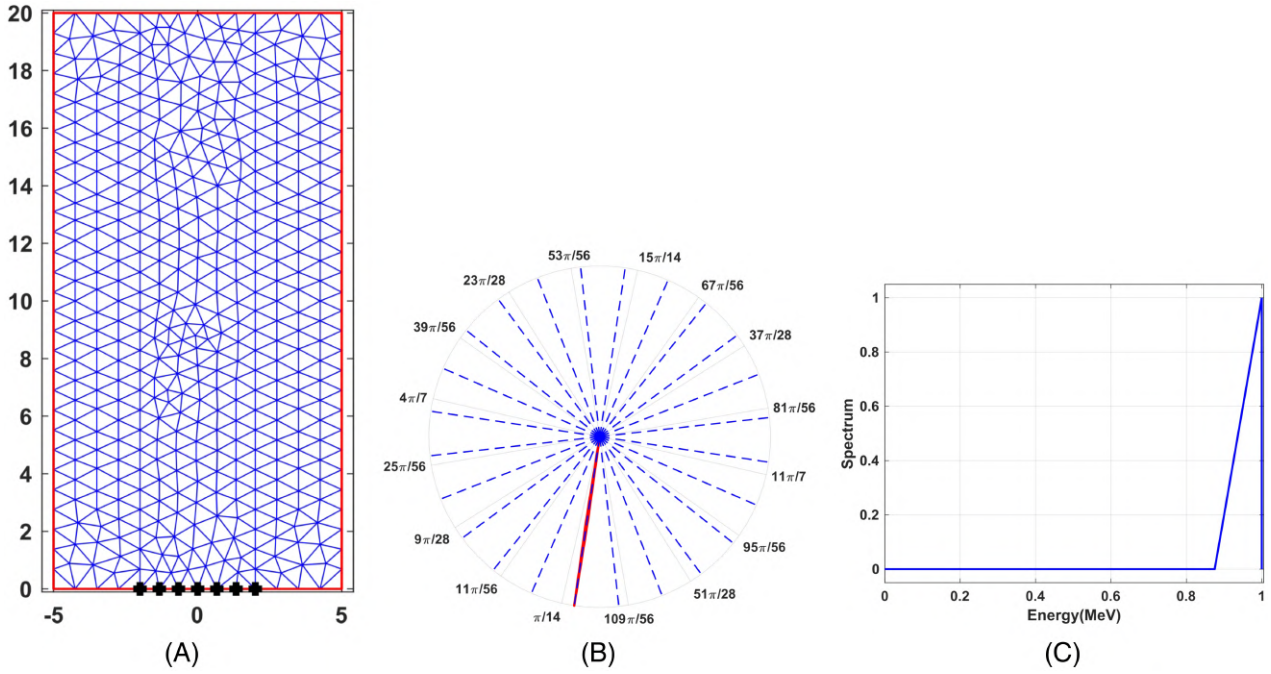
FIGURE 4 Domain discretisation. (A) Spatial discretisation of a rectangular geometry. The black dots are the points corresponding to the surface patch Γ, where the initial non-zero flux is set. (B) Angular grid defining different angular directions of photons, with the red line showing the direction along which non-zero flux, ψ_0 beam is irradiated on the surface. (C) Energy grid with different energy levels.

where $u_{i_x}^x(\mathbf{x})$, $u_{i_e}^E(E)$ and $u_{i_a}^\Omega(\Omega)$ are respectively the shape functions for spatial, energy and angular domains.

Therefore, the unknown photon flux $\psi_w(\mathbf{x}, E, \Omega)$ can be written in terms of the separable shape functions as:

$$\psi_w(\mathbf{x}, E, \Omega) = \sum_{i_x=1}^{N_1} \sum_{i_e=1}^{N_3} \sum_{i_a=1}^{N_2} \alpha_i u_{i_x}^x(\mathbf{x}) u_{i_e}^E(E) u_{i_a}^\Omega(\Omega),\tag{15}$$

where, N_1, N_2 and N_3 represent the respective nodal points in spatial, angular and energy grids and $N = N_1 N_2 N_3$. The product in Equation (15) represents the tensor product, from which we can calculate the index $i, i = 1, 2, \cdots, N$ as $i = i_a + (i_e - 1)N_2 + (i_x - 1)N_2 N_3$. Using the separable basis functions, the linear matrices in 2D can be defined as:

$$A_1(j,i) = -\left(\int_V u_{i_x}^x \frac{\partial u_{j_x}^x}{\partial x} dV \int_0^{2\pi} \cos\theta u_{i_a}^\Omega u_{j_a}^\Omega d\theta + \int_V u_{i_x}^x \frac{\partial u_{j_x}^x}{\partial y} dV \int_0^{2\pi} \sin\theta u_{i_a}^\Omega u_{j_a}^\Omega d\theta \right) \int_I u_{i_e}^e u_{j_e}^e dE,$$

$$A_2(j,i) = \left(\int_{\partial V} u_{i_x}^x u_{j_x}^x dx \int_0^{2\pi} (\Omega \cdot \mathbf{n})_+ u_{i_a}^\Omega u_{j_a}^\Omega d\Omega \right) \int_I u_{i_e}^e u_{j_e}^e dE,$$

$$A_3(j,i) = K \int_V u_{i_x}^x u_{j_x}^x dV \int_0^{2\pi} u_{i_a}^\Omega u_{j_a}^\Omega d\Omega \int_I u_{i_e}^e u_{j_e}^e dE,$$

$$A_4(j,i) = \delta \left(\int_V \frac{\partial u_{i_x}^x}{\partial x} \frac{\partial u_{j_x}^x}{\partial x} dV \int_0^{2\pi} \cos^2\theta u_{i_a}^\Omega u_{j_a}^\Omega d\theta + \int_V \frac{\partial u_{i_x}^x}{\partial x} \frac{\partial u_{j_x}^x}{\partial y} dV \int_0^{2\pi} \cos\theta \sin\theta u_{i_a}^\Omega u_{j_a}^\Omega d\theta \right.$$

$$\left. + \int_V \frac{\partial u_{i_x}^x}{\partial y} \frac{\partial u_{j_x}^x}{\partial x} dV \int_0^{2\pi} \cos\theta \sin\theta u_{i_a}^\Omega u_{j_a}^\Omega d\theta + \int_V \frac{\partial u_{i_x}^x}{\partial y} \frac{\partial u_{j_x}^x}{\partial y} dV \int_0^{2\pi} \sin^2\theta u_{i_a}^\Omega u_{j_a}^\Omega d\theta \right) \int_I u_{i_e}^e u_{j_e}^e dE,$$

$$A_5(j,i) = K\delta \left(\int_V u_{i_x}^x \frac{\partial u_{j_x}^x}{\partial x} dV \int_0^{2\pi} \cos\theta u_{i_a}^\Omega u_{j_a}^\Omega d\theta + \int_V u_{i_x}^x \frac{\partial u_{j_x}^x}{\partial y} dV \int_0^{2\pi} \sin\theta u_{i_a}^\Omega u_{j_a}^\Omega d\theta \right) \int_I u_{i_e}^e u_{j_e}^e dE, b_1(j)$$

$$= \left(\int_\Gamma \psi_0 u_{j_x}^x dx \int_0^{2\pi} (\Omega \cdot \mathbf{n})_- u_{i_a}^\Omega u_{j_a}^\Omega d\Omega \right) \int_I u_{i_e}^e u_{j_e}^e dE.$$

As noted before, the method of separable shape functions allows us to independently compute small matrices in spatial, angular and energy domains, after which we combine them to form a linear system that is in turn solved for the nodal values.

We solve the resulting linear system of Equation (8) in MATLAB using the generalised minimal residual method[42,43] on an Intel (R) Core (TM)i7 desktop office computer with CPU 3.30 GHz and 32.0 GB of RAM. For coarse mesh, the computation of smaller matrices in spatial, angular and energy domains take a few minutes, and thereafter generating the linear matrix A and solution for the whole problem was in order of few hours. The advantage of separable shape functions and mesh-free solvers for linear system is that the linear matrices may be generated independently on a personal computer, written to a file and hence use high performance computer (HPC) to solve the resulting system. For the interested readers, please see the work of References 16,17. For the large cohort of tumours and finer grid meshes, one can employ parallelization technique, using matrix-free methods, available in the portable, extensible toolkit for scientific computation (PETSc) library; however, this was beyond the scope of this study, hence not used.

Having obtained the particle flux $\psi(\mathbf{x},E,\Omega)$, we continue to calculate the energy or dose absorbed into the tumour. Following our assumption of low energy photon beam with isotropic scattering, we can assume that the energy released by photon flux is absorbed locally and hence, the dose absorbed may be calculated based on the total energy released per unit mass at the primary photon interaction point.[34] We therefore define the absorbed dose by

$$D(\mathbf{x}) = \int_I \frac{\mu}{\rho}(\mathbf{x},E) \int_S \psi(\mathbf{x},E,\Omega) d\Omega dE, \tag{16}$$

where $\rho(x)$ is the spatially dependent density of the tumour and $\frac{\mu}{\rho}(\mathbf{x},E)$ defines mass attenuation coefficient at the spatial position $\mathbf{x}$. The tabulations of mass attenuation coefficient rely on theoretical values of the total cross-sections per atom. Therefore, here we used the same cross-sectional data shown in Figure 3. To calculate the spatially dependent density, we assumed that the tumour heterogeneous density is proportional to the cellularity ratio, say $c(x), (0 \le c(x) \le 1)$. That is, we assume that the density $\rho(x) = k \cdot c(x)$, where k is some constant. Since our interest is to investigate the effect of heterogeneous characteristics in dose calculations, and since we consider heterogeneity arising from cellularity, for simplicity we take $k = 1$ which allows us to use cellularity to represent the tumour density.

3 | EXAMPLES OF APPLICATION

In this section, we describe examples of application of RT simulation by solving the LBTE equation together with the corresponding boundary condition (2), and hence dose calculation via Equation (16), in ideal geometries in 2D and 3D, and in two real cases of tumour with a single source or two sources of radiation, placed close to the defined patches on the tumour boundary. In numerical simulations, we used theoretical parameters, and assumed that the domains are composed of homogeneous materials (for the ideal 2D and 3D geometries), hence constant density. With this assumption, the absorbed dose is just a scaled particle flux in the medium. Henceforth, we present results as relative doses within a medium. To perform the simulation, we first identify the front and rear boundaries of the domain. On the front boundary, we identify a patch, where a radiation source with, $\psi = \psi_0$ is placed such that $\psi_0 = 0.027$ and set $\psi_0 = 0$ on the rest of the front boundary, with no radiation source. We assume that the rear boundary is open and that photons can leave freely but cannot re-enter the domain, hence no boundary conditions are set on ∂V_2. All simulations are performed in MATLAB.[44]

3.1 | A benchmark problem in 2D and 3D

To begin with, we consider a 2D ideal geometry composed of homogeneous material, hence constant density. Here, Equation (2) was simulated on a $[-5,5] \times [0,20]$ sq. units rectangular domain consisting of water and discretized into triangular meshes as shown in Figure 4A. For simplicity, we assume that the radiation source, and hence the incoming beam of photon is located at the centre of the front boundary such that the boundary, Γ which is the interval $[-2,2]$, shown with black dots in Figure 4A. The spatial grid is divided into $N_1 = 462$ nodes. In order to apply separable shape functions, we divided the angular domain, $[0,2\pi]$ into $N_2 = 30$ nodes while energy domain is divided into $N_3 = 10$

nodes, hence the total number of nodes for 2D simulation are $N = 138600$. In the simulations, we assumed an incoming beam of photons travelling in the direction $\Omega = (0, 1)$ and with energy 1 as shown in Figure 4C.

Similarly, we considered a 3D ideal geometry consisting of homogeneous materials hence implying constant density. The simulation was performed on a cubic domain with dimension $[-1, 4] \times [0, 5] \times [-1, 4]$ cubic units, consisting of water. The domain is discretized using tetrahedron meshes in MATLAB consisting of $N_1 = 1811$ spatial nodes. The angular domain, which is the surface of a sphere was divided into $N_2 = 20$ nodes while the energy interval divided into $N_3 = 10$ nodes, hence the total number of nodes for this simulation being $N = 362200$. We assumed an initial photon flux, $\psi_0 = 0.027$ on the surface at the centre of the cube, on the front boundary and travelling in the negative z-direction, that is the initial flux direction is, $\Omega = (0, 0, -1)$, which has an initial energy of 1. We, therefore, solved Equation (2) to get the photon flux distribution in the domain, from which we calculate the dose absorbed based on Equation (16). All the doses are normalised as will be seen under the results in Section 4.

3.2 | Modelling a real tumour under a single irradiation beam

Here, we describe the application example of two real cases of tumour, that is, DIPG and NB tumour, irradiated by a single source of incoming beam of photons, and hence describing the dose distribution within them.

DIPG tumour under a single irradiation beam: We assumed a patch Γ, around which the source of radiation is placed, and on which we assume an initial beam of photon flux travelling with velocity $\Omega = (0.989, 0.149, 0)$ and having energy 1. First, the tumour is homogeneous with constant density, and we calculate the absorbed dose by considering a single beam of incoming photon flux on the boundary section, Γ. Second, a real DIPG tumour is considered and we illustrate the dose distribution assuming heterogeneous properties in the domain. Here, we assumed that heterogeneity relates to the cell densities within the tumour, which is proportional to the heterogeneous cellularity shown in Figure 1. Hence, the spatially dependent density, $\rho(\mathbf{x})$ is proportional to cellularity. The real case of DIPG tumour used here was obtained at the diagnosis stage studied in the context of PRIMAGE project.[25] The spatial domain was divided into 8596 tetrahedron elements and $N_1 = 1982$ nodes. The angular domain was divided into $N_2 = 25$ nodes while energy domain was divided into $N_3 = 9$ nodes, implying the total number of nodes for this simulation was $N = 445950$. See results obtained in Section 4, top panel of Figure 7 to visualise the location of the boundary patch, Γ (yellow region) on which the tumour is irradiated.

NB tumour under a single irradiation beam: Similarly, on the NB tumour, we also assumed an initial beam of photon flux travelling with the velocity $\Omega = (0.0782, 0.1355, 0.9877)$ and having energy 1. First, the tumour is homogeneous with constant density, and we calculate the absorbed dose by considering one patch of tumour irradiation, which represents the point at the influx of beam of photons into the tumour. Second, we consider a realistic case to illustrate the dose distribution assuming heterogeneous properties in the tumour domain. We use heterogeneous cellularity shown in the top panel of Figure 1. The NB tumour used was obtained in the context of PRIMAGE project. The spatial domain was divided into 6077 tetrahedron elements and $N_1 = 1591$ nodes. The angular domain was divided into $N_2 = 25$ nodes while energy domain was divided into $N_3 = 9$ nodes, implying the total number of nodes for this simulation was $N = 357975$. See results obtained in Section 4 in Figure 7 to visualise the patch shown in yellow region.

3.3 | Modelling a real tumour under two irradiation beams

To illustrate the dose distribution with multiple radiation sources, hence multiple irradiation beams, we considered a real tumour irradiated by different sources of photons at different parts of the boundary of the domain. In particular and for illustrative purposes, we consider two patches, say Γ_1 and Γ_2, around which sources of radiation are placed. For a real scenario, one would have to consider possibly many beams of flux, with different initial energy spectra and at different locations on the domain boundary. The choice of these patches (beam locations) should be motivated by the composition of tumour, to ensure that the irradiation focuses on areas with high density of tumour cells (high cellularity) to be destroyed.

DIPG tumour under two irradiation beams: As in the previous case of a single source of photon beam, the tumour was divided into 8596 tetrahedron elements and $N_1 = 1982$ nodes. The angular domain was divided into $N_2 = 25$ nodes while energy domain was divided into $N_3 = 9$ nodes, implying the total number of nodes for this simulation was $N = 445950$. The simulation was performed with two irradiation beams to calculate photon flux in the domain.

Thereafter, the deposited dose was calculated based on Equation (16). In each of the two patches, the initial flux $\psi_0 = 0.027$ was set travelling with the energy 1. The first patch considered here is similar to the single patch considered in the previous subsection, where the initial beam of flux $\psi_0 = 0.027$ travels with velocity $\Omega = (0.989, 0.149, 0)$, while for the second patch, the initial incoming beam of photon flux direction is $\Omega = (0.212, -0.453, 0)$. The locations of these patches can be viewed in Section 4, in top panel of Figure 8A.

NB tumour under two irradiation beams: We consider a NB tumour irradiated from two different sources of radiation, hence two different beams of photons. For this tumour, we select Γ_1 and Γ_2 in regions with high cellularity (top panel of Figure 1). Similar to the case of a single source, the NB tumour was divided into 6077 tetrahedron elements and $N_1 = 1591$ nodes. The angular domain was divided into $N_2 = 25$ nodes while energy domain was divided into $N_3 = 9$ nodes, implying the total number of nodes for this simulation was $N = 357975$. The simulation was performed in a similar fashion to the DIPG case, and hence the deposited dose calculated based on Equation (16). In the two patches, we set the initial flux $\psi_0 = 0.027$ travelling with the relative energy 1. For the first patch, we set the initial beam of flux travelling with velocity $\Omega = (0.0.0782, 0.1355, 0.9877)$, while in the second patch, the initial beam of flux $\psi_0 = 0.027$ travels with the velocity $\Omega = (0.3909, 0.6771, -0.6235)$. The locations of these patches can be viewed in the result Section 4, in bottom panel of Figure 8D.

4 | RESULTS

In this section, we describe the results of application of BTE in ideal geometries in 2D and 3D and in real clinical cases of tumour. For a real tumour, we describe the results separately considering that the tumour is irradiated by a single source of beam or two sources of beams of photons placed close to the tumour for the case of brachytherapy. Additionally, we also present results considering tumour composed of homogeneous and heterogeneous cellularity distributions, allowing us to study the effects of heterogeneity associated with cellularity.

4.1 | A benchmark problem in 2D and 3D ideal geometries

Figure 5 shows the results of the solutions of Equation (2) on a 2D domain, starting with the initial flux, $\psi_0 = 0.027$. Since we used theoretical parameters to illustrate the application of this method, the dose distribution here is normalised, hence lies in the interval $(0, 1)$. The particle flux, and hence dose decreases as one moves towards the rear of the domain (in other words, the particle flux decreases with increasing depth), as shown in Figure 5A. The particle flux is symmetric along the x-direction (width of the domain), which is consistent with previous published works.[15–17]

Figure 6 shows the relative dose distribution in the 3D domain composed of homogeneous material with constant density. The radiation source is placed at the centre of the front boundary, hence on this boundary, we set initial flux, $\psi_0 = 0.027$ travelling parallel to the z-direction. There is no source of photons at the other boundaries, hence we set to zero initial flux on the remaining front boundary, to ensure that particles influx is only through the boundary patch, Γ.
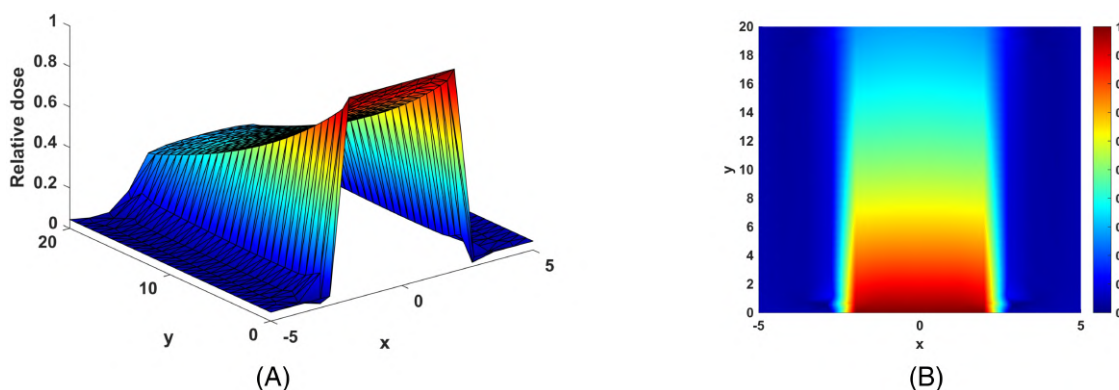

FIGURE 5 Results for the 2D simulation. (A) The relative dose distribution in a 2D geometry, while, (B) is the colour map of the absorbed dose viewed in xy plane.
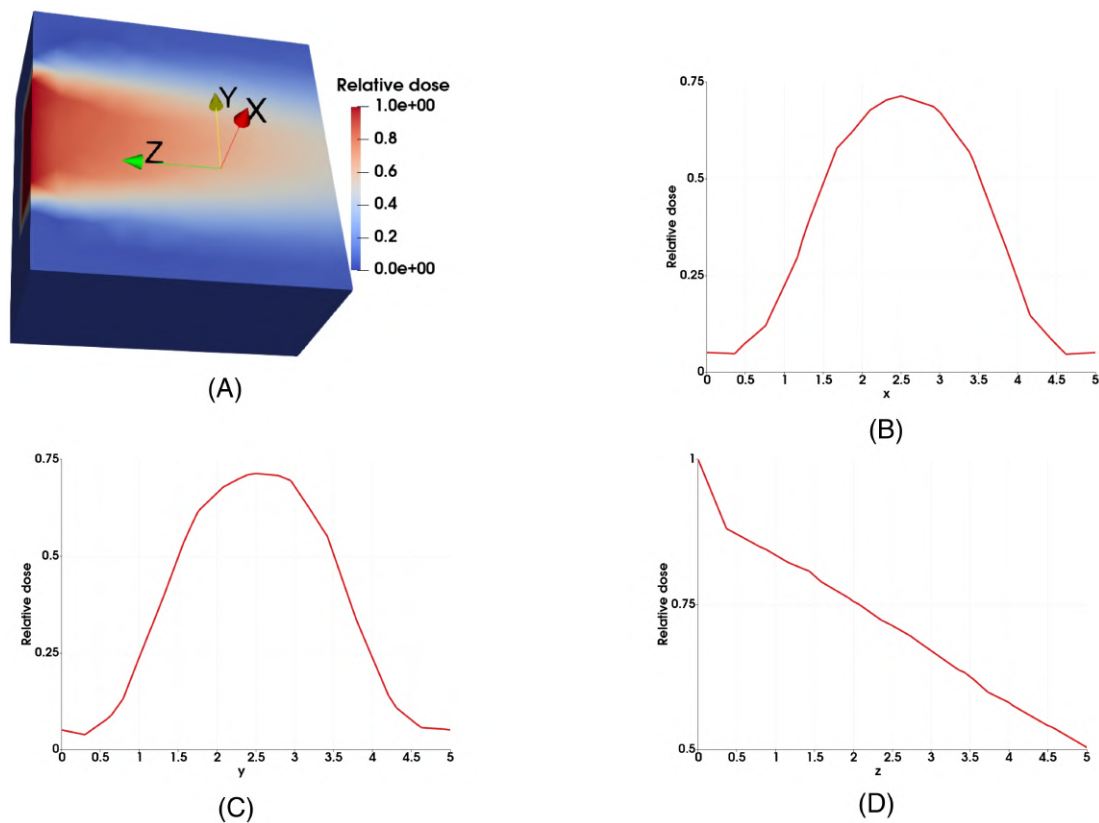
FIGURE 6 Results for the 3D simulation showing, (A) the normalised dose distribution in a cubic geometry, and along coordinate axes, cut through the 3D geometry; (B) the dose along the *x*-axis direction; (C) the dose along the *y*-axis; (D) the dose along the *z*-axis.

As expected, the absorbed dose decreases with increasing depth of the domain. To show the distribution inside the cube, we cut a section through it as shown in Figure 6A.

Figure 6B–D shows the normalised dose distributions along the coordinate axes extracted from the dose distribution in the domain shown in Figure 6A. The dose is distributed symmetrically along the *x* and *y* directions as shown in Figure 6B,C. The two axes lie in a plane perpendicular to the particle flux direction, and the shown results are consistent to the results in the literature. On the other hand, along the *z*-direction, the dose distribution decreases as one moves towards the rear boundary of the domain, which is again consistent with previous published works.[15–17] These test problems allow us to check the applicability of the model to compute the dose in the real geometries from DIPG and NB tumours.

To validate the reliability of our model, we conducted benchmark tests in both 2D and 3D domains. These results were then qualitatively compared with findings reported in published literature. Notably, Boman et al[16,17] demonstrated a decrease in absorbed dose with increasing depth of the domain, a trend consistent with the results depicted in Figures 5 and 6. Moreover, our observations align with the findings of Das and Pouso,[13] indicating a symmetric distribution along the transverse directions. These consistent findings also reinforce the validity of our model, as seen in similar studies conducted by Tervo et al[15,38] and numerous other published works.

4.2 | Tumour irradiation with a single beam of photons

Figure 7 top panel shows results of relative dose distribution within a real case of DIPG by considering a single patch, around which the radiation is placed for brachytherapy, hence the source from which the tumour is irradiated. The patch Γ is shown in yellow colour in Figure 7A. On Γ, we assumed that a non-zero beam of photon, $\psi_0 = 0.027$ travelling in direction parallel to the vector $\Omega = (0.9888, 0.1490, 0)$, while in all other directions, there is no radiation source, hence no incoming beam of photons, thus we set the incoming flux velocity to zero. Similarly, the incoming flux has
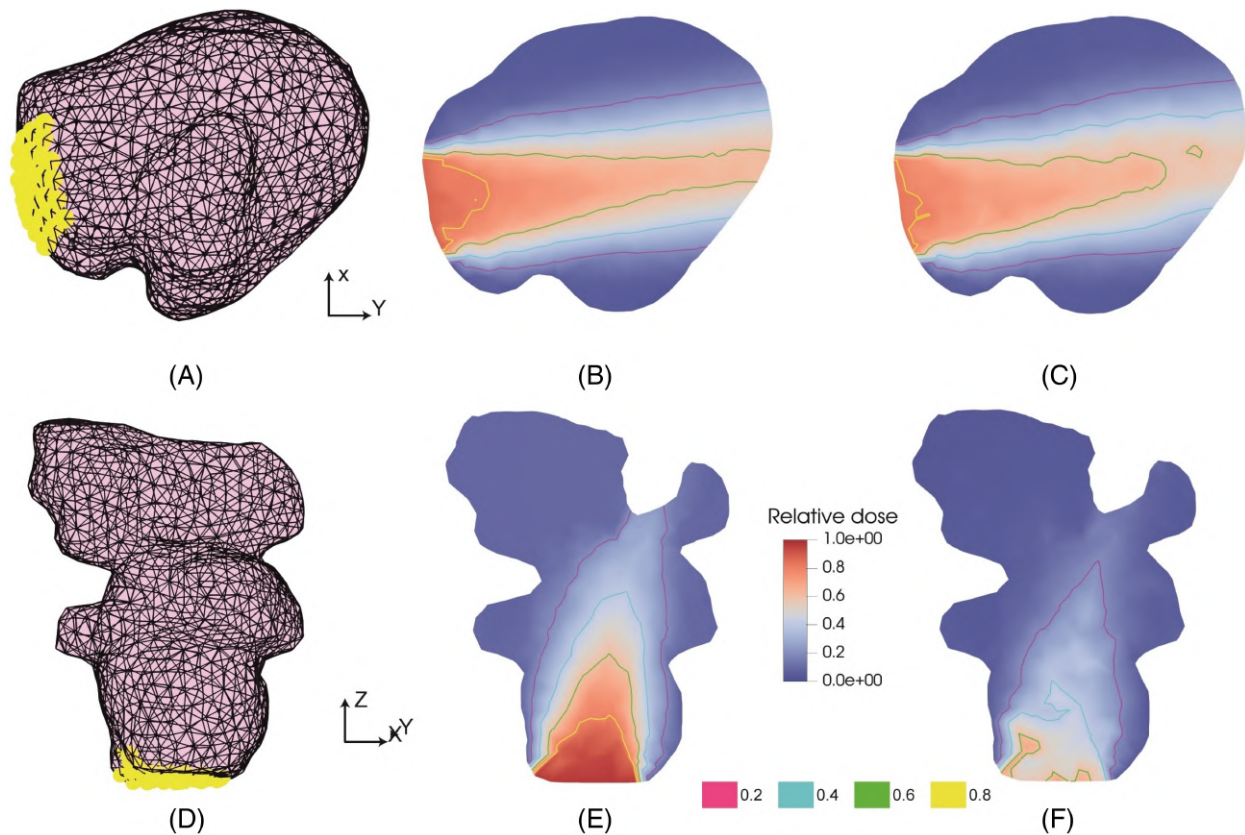
FIGURE 7 Dose distribution in real geometries of DIPG and NB tumours irradiated from a single patch. Top panel: DIPG tumour; (A) meshed geometry with an initial patch shown in yellow; (B) dose distribution considering homogeneous DIPG tumour properties; (C) dose distribution considering heterogeneous DIPG tumour properties. Bottom panel: NB tumour; (D) geometry with an initial patch shown in yellow; (E) dose distribution considering homogeneous NB tumour properties; (F) dose distribution considering heterogeneous NB tumour properties. Figures (B–F) are cut views corresponding to the mid-plane. DIPG, diffuse intrinsic pontine glioma; NB, neuroblastoma.

energy spectrum of 1 MeV, which decreases to zero at all the remaining energy levels. Figure 7B,C shows the dose distribution considering homogeneous and heterogeneous properties of DIPG, respectively. The absorbed dose decreases in the x direction, while it is symmetrically distributed along the y and z-directions. On the figures, we also show the isocurve (dose contour) for different values of dose in the domain. These curves depict the differences and effect of the heterogeneous properties. The cellularity is not so much heterogeneous in a DIPG tumour, hence the slight differences in the dose computed in both cases.

Figure 7 bottom panel shows relative dose distribution in a real case of NB tumour, considering a single patch of tumour irradiation. The irradiation patch Γ is shown in yellow colour in Figure 7D, where we set a non-zero flux, $\psi_0 = 0.027$, travelling with the velocity $\Omega = (0.0782, 0.1355, 0.9877)$, while in all other directions, the incoming flux velocity is set to zero. Similarly, the incoming flux has energy spectrum of 1 MeV, which decreases to zero at all the remaining energy levels. Figure 7E,F shows the dose distribution considering homogeneous and heterogeneous properties of NB tumour, respectively. The isocurves (dose contour) are plotted for different values of dose in the domain of NB tumour. These curves depict the differences and effect of the heterogeneous properties. NB tumour is relatively heterogeneous compared to DIPG and hence noticeable differences in the dose distribution.

In this section, we have presented the results of the application of BTE to real clinical cases of DIPG and NB tumours irradiated by a single beam of photons or photon beams from two boundary sections referred to here as patches. The application here considered two cases: assumption of homogeneous and heterogeneous properties in both tumours, to illustrate the effect of varying tumour density on the dose deposited during RT treatment. Heterogeneity properties influence dose deposited as can be seen from Figure 7. As shown from Figure 1, the cellularity distribution is more heterogeneous in a NB tumour than DIPG, and we can see this effect highlighted in the results; there is noticeable differences between dose calculation in a NB tumour, considering homogeneous and heterogeneous properties, than
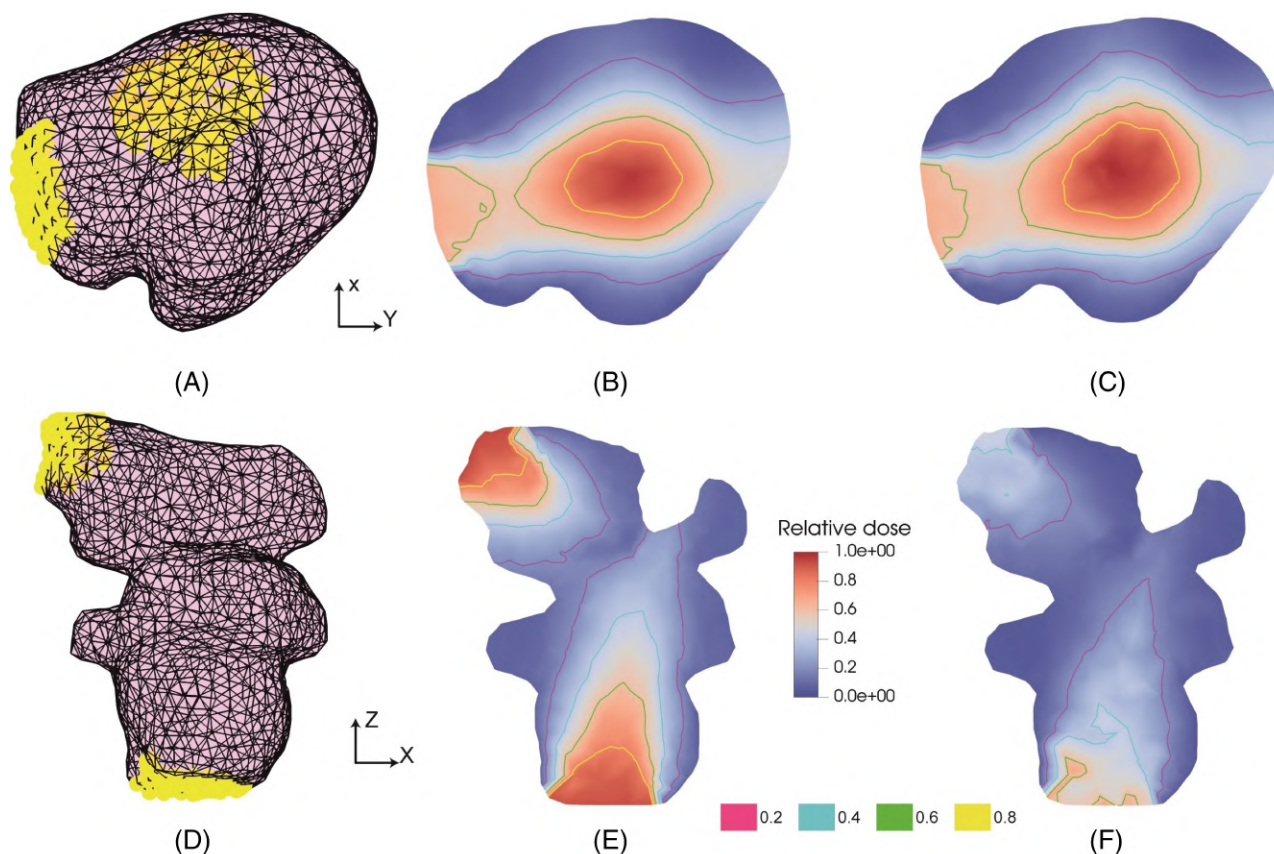
FIGURE 8 Dose distribution within real geometry of DIPG and NB tumours considering two patches. Top panel: DIPG tumour (A) two patches shown in yellow; (B) dose distribution considering homogeneous properties of DIPG; (C) dose distribution considering heterogeneous properties of DIPG tumour. Bottom panel: (D) patches of NB tumour irradiation shown in yellow; (E) dose distribution considering NB homogeneous properties; (F) dose distribution considering NB heterogeneous properties. Figures (B–F) are cut views corresponding to the mid-plane. DIPG, diffuse intrinsic pontine glioma; NB, neuroblastoma.

there is observed in the case of DIPG tumour. Following the results for a single source of photon beam, we next proceed to calculate the absorbed dose for a tumour irradiated by photon beams from two sources at two different locations on boundary. We to refer to these as patches Γ_1 and Γ_2.

4.3 | Tumour irradiation with two beams of photons

Next, we consider the application results where the tumour is irradiated with two radiation sources, producing beams of low energy photons travelling in different directions and at different locations on the tumour boundary, highlighting also the effect of heterogeneity. This case illustrates the idea of irradiating a tumour with different beams of particles at different locations and with different energies as the linear accelerator machine rotates throughout the radiation process to deliver dose from different points and through different angles (directions). We remark here that we only considered two beams to illustrate the concept. However, for a realistic case, several beams with different beam directions and energies should be considered.

For the DIPG tumour, two different patches Γ_1 and Γ_2 were chosen on the boundary as shown in Figure 8A and then we assume that radiation sources of photons are placed close to these patches, hence the tumour irradiated through the selected patches with two different photon beams. On these patches, we set the incoming beams of fluxes, $\psi_0 = 0.027$ travelling with velocities $\Omega = (0.989, 0.149, 0)$ and $\Omega = (0.212, -0.453, 0.866)$, respectively. Thereafter, integrated photon flux within the tumour domain and hence dose distribution for both the homogeneous and heterogeneous material was obtained as shown in Figure 8. Figure 8B shows dose distribution in the DIPG tumour considering homogeneous material while (Figure 8C) the corresponding distribution in a heterogeneous DIPG tumour, with the

isocurves (contours) plotted to illustrate the differences in the two distributions. The bottom panel of Figure 8 shows the results of application of BTE to NB tumour considering two irradiation beams, as shown in Figure 8D. Here, we set the incoming beam of flux, $\psi_0 = 0.027$ travelling with velocities $\Omega = (0.0782, 0.1355, 0.9877)$ and $\Omega = (0.3909, -0.6771, -0.6235)$, respectively. Thereafter, the photon fluxes in NB tumour were integrated both for the homogeneous and heterogeneous properties as shown in Figure 8. Figure 8E shows dose distribution considering homogeneous material while (Figure 8F) the corresponding distribution in a heterogeneous properties in the NB tumour, with the isocurves (contours) plotted to illustrate the differences in the two distributions.

This part summarises the results of application of BTE to DIPG and NB tumour irradiated at two patches; assuming tumour properties being both homogeneous and heterogeneous. As highlighted above and also as considered for a single patch, heterogeneity properties influence dose deposited within the tumour domains as shown in Figure 8. Due to cellularity heterogeneity observed in NB tumour, we see a clear distinction between the dose deposited considering homogeneous and heterogeneous properties. These differences are more clear and pronounced as compared to the DIPG tumour with less heterogeneous properties.

To analyse the impact of cellularity on computed dose, we calculated the discrepancy between dose distributions in homogeneous and heterogeneous cases for both DIPG and NB tumours. Furthermore, we computed the correlation coefficient between the dose difference and cellularity values. Figure 9 presents histograms depicting the dose differences in homogeneous and heterogeneous tumours, along with a histogram of cellularity values. Additionally, each figure includes the corresponding correlation coefficient between the dose difference and cellularity.

Figure 9A,B displays histograms representing the DIPG tumour. For a single patch, the correlation coefficient between the dose disparity and cellularity is approximately -0.54, while for two patches, the correlation coefficient increases to -0.77. The presence of heterogeneity in the dose disparity suggests an external input that contributes to this non-uniformity. One of the factors influencing this heterogeneity is cellularity, which exhibits a negative correlation with the dose differences. As we transition from the single-patch case to the cumulative case involving two patches, the correlation coefficient increases. However, the correlation coefficient is not notably high due to the existence of nodes with no photon flux, which remain unaffected even with the introduction of heterogeneity. This observation also explains the enhanced correlation coefficient in the cumulative case, as the number of nodes with no photon flux decreases.

In the case of the NB tumour, as shown in Figure 9C,D, a similar observation is made. However, there is no significant correlation observed, mainly due to a significant number of nodes with zero photons compared to the DIPG tumour. Additionally, we observe a wider spread of dose differences in comparison to the DIPG case, where the values are more closely clustered. This wider spread can be attributed to the greater heterogeneity in NB cellularity compared to DIPG cellularity as we saw in Figure 1.

In this section, we have presented at the results of application of photon transport, modelled through BTE to dose calculation. A benchmark problem tested the validity of our approach, thereafter, we simulated the dose distribution in real cases of DIPG and NB tumour considering a single beam and two beams of tumour irradiation, in both cases, incorporating both homogeneous and heterogeneous properties. The simulations help us to note the differences in dose calculation, which is dependent on tumour properties, as well as highlighting the dose distribution differences in different tumours with different characteristics. To be more specific, in both cases of irradiating a tumour either by a single beam
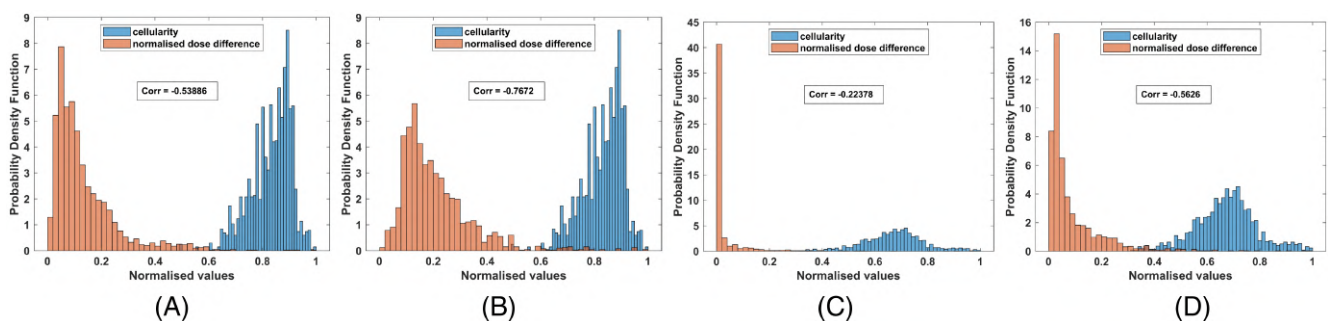

FIGURE 9 Comparison of dose differences with cellularity distribution. (A) DIPG tumour considering particle source from a single patch; (B) DIPG tumour considering particle source from two patches; (C) NB tumour considering particle source from a single patch; (b) NB tumour considering particle source from two patches. DIPG, diffuse intrinsic pontine glioma; NB, neuroblastoma.

or two beams of photon fluxes, DIPG tumour presents less differences between dose distribution considering homogeneous and heterogeneous properties, as shown in Figures 7B,C and 8B,C; on the contrary, NB tumour presents much more clear differences between dose distribution considering homogeneous and heterogeneous properties as shown in Figures 7E,F and 8E,F. These differences and influence of heterogeneity is highlighted in Figure 9. We noted correlation coefficient between the dose disparity for homogeneous and heterogeneous cases with the cellularity. The correlation increased when we considered cumulative case of radiation sources from two patches. These differences in the dose distributions in the two types of tumours correlate to the cellularity data shown in Figure 1, showing different heterogeneous characteristics between DIPG and NB tumours. DIPG presents a more homogeneous cellularity distribution, which justifies the reason as to why RT is much more effective in DIPG tumour than in the NB tumour, where chemotherapy is combined with RT.

5 | DISCUSSION AND CONCLUSION

In order to simplify models for dose calculation while increasing accuracy, a lot of studies have focused on the use of deterministic dose calculation models as an alternative method to Monte Carlo approach that is widely used in RT clinical treatment planning.[18,45–47] More specifically, the studies have focused on directly modelling the transport of radiative particles (electrons, photons, etc.) through the use of BTEs[48,49] and in addition approximating their solutions as accurately as possible.[8,15,16] Therefore, in this work, we focused on the investigation of the effect of tumour heterogeneous properties on the dose calculation in real cases of cancer, through the solution of BTE of photons. This simplified model has been used here as a proof-of-concept to the investigation of the effect of heterogeneous properties on dose deposited within real tumours following a future deterministic model of coupled transport equations for electrons and photons. In this work, we first described the BTE model for photons and its numerical implementation via continuous FEM on all variables, on ideal geometries in 2D and 3D, as a benchmark problem to test the validity of our approach. Furthermore, we also implemented this model in real geometries and hence calculated the dose absorbed in real clinical cases of DIPG and NB tumours obtained from PRIMAGE data set, within the context of PRIMAGE.[25] In a first approach, the real problem was solved considering that the tumour is homogeneous; next, we incorporated the tumour heterogeneous properties into the dose calculation model. This study has thus used this simplified model of photons as a proof-of-concept to highlight the importance of incorporating the heterogeneous properties. Our future studies will be built upon this work, where the tumour and tissue properties are integrated into the dose models, hence allowing us to model real cases of tumour with heterogeneous properties. In previous studies, several numerical techniques, including expansion in orders of scattering, FE and finite difference methods for the spatial variables, multi-group methods for the energy variable, discrete ordinate methods for the angular variables, were used to simulate the transport of radiative particles, while other works applied FEM to all the variables to approximate the solution of BTE[15–17,29] and found very good agreement with Monte Carlo method. Our study here extended the last ones by applying FEM to all the variables and in turn applying this to clinical cases of DIPG and NB tumour, by incorporating the change in material densities based on the patient specific data extracted from MRI images and extrapolated on a 3D mesh. Therefore, this preliminary study forms the foundation upon which we build our future study of integrating particle (electrons and photons) transport model with the model of tumour growth to fully characterise and simulate RT treatment of DIPG cases and a case of a tumour that also requires RT as an additional means of treatment, as in the case of NB tumour.

To sum up; there is an evident impact of tumour heterogeneity on dose distribution, the following conclusions are made:

- The differences in dose distribution between homogeneous and heterogeneous cases are more pronounced in the NB tumour. Indeed, this tumour exhibit greater heterogeneity in cellularity compared to the DIPG tumour. These findings suggest the influence of dose distribution by factors, such as cellularity.
- Furthermore, the analysis of differences in dose distribution between homogeneous and heterogeneous cases reveal a negative correlation between dose disparity and cellularity in both tumours.
- The correlation is more prominent when considering the cumulative case involving two patches of radiation sources. However, the correlation coefficient is not significantly high due to the existence of nodes with zero particle fluxes, which remain unaffected even with the introduction of heterogeneity.

- The previous observation explains the enhanced correlation coefficient in the cumulative case, as the number of nodes with zero particle flux decreases. Overall, these findings indicate that tumour heterogeneity plays a crucial role in the non-uniformity of dose distribution.
- The differences in dose calculation and distribution observed between DIPG and NB tumours highlight the importance of considering tumour characteristics in treatment planning.
- The more homogeneous cellularity distribution in DIPG tumours may contribute to the higher effectiveness of RT alone, while the greater heterogeneity in NB tumours necessitates combining chemotherapy with RT for improved treatment outcomes.

Finally, having considered a simplified model to illustrate the effect of heterogeneity, it is limited in its applicability.

- The main assumption of this study lies in the use of BTE for photons to characterise dose distribution in tissues, ignoring main scattering events such as the Compton scattering.
- This previous assumption limits the application of this model, so to fully characterise the dose deposition problem, a full BTE coupling at least electron and photon transport is required.
- The use of the FEM to discretize all variables needed to solve the BTE requires the use of fine FE meshes to reduce numerical artefacts in case of discontinuities. Nonetheless, using fine meshes can increase excessively the computational cost of the model. Therefore, to avoid these numerical issues while using a coarse mesh, we used the streamlined-diffusion method to stabilise the solution of the model. The use of discontinuous shape functions is recommended for a comprehensive model.
- The combination of the simplified isotropic scattering and the streamlined-diffusion method showed good accuracy. However, when modelling the full transport problem (including all scattering events), finer meshes would be required to obtain accurate results. To reduce the computational cost associated with these finer meshes, parallelized mesh-free methods could be employed (see e.g., Reference 17 for illustration of such an algorithm).

Therefore, this study presented a simplified deterministic model for dose calculation, focusing solely on the transport of photons. It serves as a proof-of-concept study, illustrating the impact of heterogeneous tumour properties on a comprehensive RT treatment planning model.

CONFLICT OF INTEREST STATEMENT
The authors declare no conflict of interest.

DATA AVAILABILITY STATEMENT
The data that support the findings will be available in Zaguan at https://zaguan.unizar.es following an embargo from the date of publication to allow for commercialization of research findings.

ORCID
Victor Ogesa Juma https://orcid.org/0000-0002-9832-0955
Diego Sainz-DeMena https://orcid.org/0000-0001-7452-0437
María Teresa Sánchez https://orcid.org/0000-0002-3514-6443
José Manuel García-Aznar https://orcid.org/0000-0002-9864-7683

REFERENCES
1. Berlanga P, Cañete A, Castel V. Advances in emerging drugs for the treatment of neuroblastoma. *Expert Opin Emerg Drugs*. 2017;22(1): 63-75. doi:10.1080/14728214.2017.1294159

2. Gong L, Zhang Y, Liu C, Zhang M, Han S. Application of radiosensitizers in cancer radiotherapy. *Int J Nanomed*. 2021;16:1083-1102. doi:10.2147/IJN.S290438

3. Baskar R, Lee KA, Yeo R, Yeoh KW. Cancer and radiation therapy: current advances and future directions. *Int J Med Sci*. 2012;9(3): 193-199. doi:10.7150/ijms.3635

4. Duclous R, Dubroca B, Frank M. A deterministic partial differential equation model for dose calculation in electron radiotherapy. *Phys Med Biol*. 2010;55(13):3843-3857. doi:10.1088/0031-9155/55/13/018

5. Jabbari K. Review of fast Monte Carlo codes for dose calculation in radiation therapy treatment planning. *J Med Signals Sens*. 2011; 1(1):73.

6. Gifford KA, Horton JL, Wareing TA, Failla G, Mourtada F. Comparison of a finite-element multigroup discrete-ordinates code with Monte Carlo for radiotherapy calculations. *Phys Med Biol*. 2006;51(9):2253-2265. doi:10.1088/0031-9155/51/9/010

7. Vassiliev ON, Wareing TA, McGhee J, Failla G, Salehpour MR, Mourtada F. Validation of a new grid-based Boltzmann equation solver for dose calculation in radiotherapy with photon beams. *Phys Med Biol*. 2010;55(3):581-598.

8. Börgers C. Complexity of Monte Carlo and deterministic dose-calculation methods. *Phys Med Biol*. 1998;43(3):517-528. doi:10.1088/0031-9155/43/3/004

9. Olbrant E, Frank M. Generalized Fokker–Planck theory for electron and photon transport in biological tissues: application to radiotherapy. *Comput Math Methods Med*. 2010;11(4):313-339. doi:10.1080/1748670X.2010.491828

10. Papanikolaou N, Stathakis S. Dose-calculation algorithms in the context of inhomogeneity corrections for high energy photon beams. *Med Phys*. 2009;36(10):4765-4775. doi:10.1118/1.3213523

11. Vassiliev ON. *Monte Carlo Methods for Radiation Transport*. Fundamentals and Advanced Topics; 2017.

12. St. Aubin J, Keyvanloo A, Fallone B. Discontinuous finite element space-angle treatment of the first order linear Boltzmann transport equation with magnetic fields: application to MRI-guided radiotherapy. *Med Phys*. 2016;43(1):195-204.

13. Das TK, Pouso ÓL. New insights into the numerical solution of the Boltzmann transport equation for photons. *Kinet Relat Models*. 2014; 7(3):433-461. doi:10.3934/krm.2014.7.433

14. Lewis, E.E., Miller, W.F. *Computational methods of neutron transport*. John Wiley and Sons, Inc.; 1984.

15. Tervo J, Kolmonen P, Vauhkonen M, Heikkinen L, Kaipio J. A finite-element model of electron transport in radiation therapy and a related inverse problem. *Inverse Problems*. 1999;15(5):1345-1361. doi:10.1088/0266-5611/15/5/316

16. Boman E, Tervo J, Vauhkonen M. Modelling the transport of ionizing radiation using the finite element method. *Phys Med Biol*. 2004; 50(2):265-280. doi:10.1088/0031-9155/50/2/006

17. Boman E. *Radiotherapy forward and inverse problem applying Boltzmann transport equation (Sädehoidon suora ja käänteisongelma Boltzmannin siirtoyhtälön avulla)*. Ph.D. thesis. Kuopion yliopisto; 2007.

18. Chidyagwai P, Frank M, Schneider F, Seibold B. A comparative study of limiting strategies in discontinuous Galerkin schemes for the M1 model of radiation transport. *J Comput Appl Math*. 2018;342:399-418. doi:10.1016/j.cam.2018.04.017

19. Frank M, Hauck C, Kuepper K. Convergence of filtered spherical harmonic equations for radiation transport. *Commun Math Sci*. 2016; 14(5):1443-1465. doi:10.4310/cms.2016.v14.n5.a10

20. Hensel H, Iza-Teran R, Siedow N. Deterministic model for dose calculation in photon radiotherapy. *Phys Med Biol*. 2006;51(3):675-693. doi:10.1088/0031-9155/51/3/013

21. Celora GL, Byrne HM, Kevrekidis P. Spatio-temporal modelling of phenotypic heterogeneity in tumour tissues and its impact on radiotherapy treatment. *J Theor Biol*. 2022;556:111248. doi:10.1016/j.jtbi.2022.111248

22. Mikell JK, Klopp AH, Gonzalez GM, et al. Impact of heterogeneity-based dose calculation using a deterministic grid-based Boltzmann equation solver for intracavitary brachytherapy. *Int J Radiat Oncol Biol Phys Ther*. 2012;83(3):e417-e422. doi:10.1016/j.ijrobp.2011.12.074

23. Poon E, Williamson JF, Vuong T, Verhaegen F. Patient-specific Monte Carlo dose calculations for high-dose-rate endorectal brachytherapy with shielded intracavitary applicator. *Int J Radiat Oncol Biol Phys Ther*. 2008;72(4):1259-1266. doi:10.1016/j.ijrobp.2008.07.029

24. Richardson S, Palaniswaamy G, Grigsby PW. Dosimetric effects of air pockets around high–dose rate brachytherapy vaginal cylinders. *Int J Radiat Oncol Biol Phys Ther*. 2010;78(1):276-279.

25. Martí-Bonmatí L, Alberich-Bayarri Á, Ladenstein R, et al. PRIMAGE project: predictive in silico multiscale analytics to support childhood cancer personalised evaluation empowered by imaging biomarkers. *Eur Radiol Exp*. 2020;4(1):1-11. doi:10.1186/s41747-020-00150-9

26. Sainz-DeMena D, García-Aznar JM, Pérez MA, Borau C. Im2mesh: a python library to reconstruct 3D meshes from scattered data and 2D segmentations. Application to patient-specific neuroblastoma tumour image sequences. *Appl Sci*. 2022;12(22):11557. doi:10.3390/app122211557

27. Atuegwu NC, Arlinghaus LR, Li X, et al. Parameterizing the logistic model of tumor growth by dw-mri and dce-mri data to predict treatment response and changes in breast cancer cellularity during neoadjuvant chemotherapy. *Transl Oncol*. 2013;6(3):256-264.

28. de Melo Quintela B, Hervas-Raluy S, Garcia-Aznar JM, Walker D, Wertheim KY, Viceconti M. A theoretical analysis of the scale separation in a model to predict solid tumour growth. *J Theor Biol*. 2022;547:111173. doi:10.1016/j.jtbi.2022.111173

29. Tervo J, Kokkonen P, Frank M, Herty M. On approximative linear Boltzmann transport equation for charged particles. *Math Models Methods Appl Sci*. 2018;28(14):2905-2939. doi:10.1142/S0218202518500641

30. Tervo J, Kokkonen P, Frank M, Herty M. On existence of solutions for Boltzmann continuous slowing down transport equation. *J Math Anal Appl*. 2018;460(1):271-301. doi:10.1016/j.jmaa.2017.11.052

31. Bedford JL. Calculation of absorbed dose in radiotherapy by solution of the linear Boltzmann transport equations. *Phys Med Biol.* 2019; 64(2):02TR01. doi:10.1088/1361-6560/aaf0e2

32. Börgers C, Larsen EW. Asymptotic derivation of the Fermi pencil-beam approximation. *Nucl Sci Eng.* 1996;123(3):343-357. doi:10.13182/NSE96-A24198

33. Pomraning G. The Fokker-Planck operator as an asymptotic limit. *Math Models Methods Appl Sci.* 1992;2(1):21-36. doi:10.1142/S021820259200003X

34. De Martino F, Clemente S, Graeff C, Palma G, Cella L. Dose calculation algorithms for external radiation therapy: an overview for practitioners. *Appl Sci.* 2021;11(15):6806. doi:10.3390/app11156806

35. Jörres C. *Numerical Methods for Boltzmann Transport Equations in Radiotherapy Treatment Planning.* Ph.D. thesis. Universitätsbibliothek der RWTH Aachen; 2015.

36. Powell CJ, Jablonski A, Salvat F. NIST databases with electron elastic-scattering cross sections, inelastic mean free paths, and effective attenuation lengths. *Surf Int Anal.* 2005;37(11):1068-1071.

37. Dautray R, Lions JL. *Mathematical Analysis and Numerical Methods for Science and Technology.* Springer Science & Business Media; 2012.

38. Tervo J, Kolmonen P. Inverse radiotherapy treatment planning model applying Boltzmann-transport equation. *Math Models Methods Appl Sci.* 2002;12(1):109-141. doi:10.1142/S021820250200157X

39. Kanschat G. *Parallel and Adaptive Galerkin Methods for Radiative Transfer Problems.* Ph.D. thesis. 1996.

40. Kanschat G. A Robust Finite Element Discretization for Radiative Transfer Problems with Scattering. *IWR*; 1998.

41. Zhou G. How accurate is the streamline diffusion finite element method? *Math Comput.* 1997;66(217):31-44. https://www.jstor.org/stable/2153641

42. Campbell SL, Ipsen IC, Kelley CT, Meyer CD. GMRES and the minimal polynomial. *BIT Numer Math.* 1996;36(4):664-675. doi:10.1007/BF01733786

43. Van der Vorst HA. *Iterative Krylov Methods for Large Linear Systems.* Cambridge University Press; 2003.

44. The MathWorks Inc. *MATLAB Version: 9.13.0 (R2022b).* The MathWorks Inc.; 2022.

45. Barnard RC, Frank M, Krycki K. Sensitivity analysis for dose deposition in radiotherapy via a Fokker–Planck model. *Math Med Biol.* 2017;34(1):109-123. doi:10.1093/imammb/dqv039

46. Frank M, Herty M, Schäfer M. Optimal treatment planning in radiotherapy based on Boltzmann transport calculations. *Math Models Methods Appl Sci.* 2008;18(4):573-592. doi:10.1142/S0218202508002784

47. Tervo J. On global existence and regularity of solutions for a transport problem related to charged particles. *J Comput Theoretical Transp.* 2021;50(3):180-219. doi:10.1080/23324309.2020.1851722

48. Frank M, Herty M, Sandjo AN. Optimal radiotherapy treatment planning governed by kinetic equations. *Math Models Methods Appl Sci.* 2010;20(4):661-678. doi:10.1142/S0218202510004386

49. Li W, Carrete J, Katcho NA, Mingo N. ShengBTE: a solver of the Boltzmann transport equation for phonons. *Comput Phys Commun.* 2014;185(6):1747-1758. doi:10.1016/j.cpc.2014.02.015